

An Agile Samara-Inspired Single-Actuator Aerial Robot Capable of Autorotation and Diving

Shane Kyi Hla Win^{ID}, Luke Soe Thura Win^{ID}, Danial Sufiyan^{ID}, Gim Song Soh^{ID}, and Shaohui Foong^{ID}

Abstract—Large scale aerial deployment of miniature sensors in tough environmental conditions requires a deployment device that is lightweight, robust, and steerable. We present a novel samara-inspired autorotating craft that is capable of two flight modes (autorotating mode and diving mode) with an average glide angle of 28.9° (1.81 m lateral distance per 1 m loss of altitude) in the former mode. The bidirectional transition between the two modes and directional control is achieved by using only a single actuator. Also, in order to minimize its glide angle, a design optimization methodology is presented for our prototype, diving samara autorotating wing, along with a new cyclic control strategy for directional control of autorotating descent. The dynamic model, simulated in a six degrees-of-freedom environment using the blade element theory, is integrated with genetic algorithm to derive parameters for the wing geometry, flap angle for autorotation, and the proposed cyclic control. The physical prototype autorotates at a descent velocity of 1.43 m/s and rotation speed 4.17 Hz, and is able to transit to diving mode in an average duration of 272 ms to increase its descent velocity by at least 17.6 times. At any point during the dive, it is able to transit back into autorotation in an average duration of 327 ms. Semioutdoor experiments were used to investigate the bidirectional transitions and verify the glide angle (28.9°), which is much improved from the previous prototype (SAW+, 58.4°). Lastly, as a demonstration of a real-life deployment scenario and environmental conditions, the prototypes were dropped from a fixed-wing unmanned aerial vehicle at a suburban test site.

Index Terms—Aerial systems, applications, biologically inspired robots, biomimetics, mechanics and control.

I. INTRODUCTION

IN MANY areas such as military, research, wildlife, and disaster rescue efforts, it is essential to deploy large numbers of lightweight sensors or payloads to desired locations as quickly as possible. In some use cases, the covertness of the deployment is critical to the success of the mission. These sensors or payloads can be air-deployed [1]–[4] using an aircraft or an unmanned aerial vehicle (UAV) (see Fig. 1). The conventional

Manuscript received October 27, 2020; revised March 24, 2021; accepted June 14, 2021. This work was supported in part by the SUTD-MIT International Design Centre (IDC) and in part by the Temasek Laboratories @ SUTD, Singapore. This article was recommended for publication by Associate Editor G. Heredia and Editor P. Robuffo Giordano upon evaluation of the reviewers' comments. (Corresponding author: Shaohui Foong.)

The authors are with the Engineering Product Development Pillar, Singapore University of Technology, and Design, Singapore 487372 (e-mail: win,hlawin_kyi@alumni.sutd.edu.sg; thura_soe@sutd.edu.sg; dss_2020@hotmail.com; sohgimsong@sutd.edu.sg; shao@sutd.edu.sg).

Color versions of one or more figures in this article are available at <https://doi.org/10.1109/TRO.2021.3091275>.

Digital Object Identifier 10.1109/TRO.2021.3091275

way to deploy sensors is either by hard-landing of ruggedized sensors [3],[4] or by the use of an arrest device such as a parachute or a guided parafoil [5],[6]. The drawback with the former is the high cost of manufacturing ruggedized sensors and the inflexibility of the flight path for deployment aircraft. With the latter, the challenge lies with the intricate packaging of the parafoil whose canopy must not collapse for a successful drop.

Bioinspired robotics, the imitation of nature's models, systems, and elements, has often helped us to solve complex human problems. Bioinspired methods are used in the UAV research [7]–[9] and in optimization algorithms such as genetic algorithm (GA) [10]. The concept proposed in this work was inspired by the falling of maple seeds [11]–[13] for aerial deployment of lightweight sensors or payloads. Similar to the biological counterpart, it utilizes autorotation to slow down its vertical descent and additionally employs a single-flap mechanism to achieve trajectory control during the autorotation.

In recent years, there have been some notable attempts at lightweight sensor delivery using samara-inspired methods. A research work by Kellas [14] described an autorotating device with a controllable vertical fin mounted at the wing tip. Trajectory controlled drop tests were inconclusive due to poor weather, short drop distance and technical difficulties. A more recent work [15] featured a samara-inspired device with an integrated electromechanical structure. This work focused on low-cost and easy manufacturing of the device, lacking trajectory control. Other works have explored using autorotation [2],[16], [17] or samara-inspired designs [18],[19], but none had the element of trajectory or directional control. This likely indicates that research interest in single-winged autorotating devices may be limited, largely due to the many challenges involved in designing a readily autorotating platform and lack of appropriate testing facilities while possible results do not appear very appealing or rewarding. A recent work by U.S. Naval Research Laboratory features a disposable sensor-carrying platform, CICADA [20], with navigation, guidance, and flight control, but its fixed-wing platform rules out vertical descent, diving, quick recovery, or soft landing. Other payload delivery or surveillance solutions [21],[22] are also in the form of fixed-wing type microair vehicles but they use on-board propulsion system for sustained flights.

Some samara-inspired platforms with on-board propulsion, called monocopters, can achieve sustained controllable flight [23]–[25]. These concepts most often use a flap that is cut-out along the main wing. Notably, there are two ways of actuating the flap for trajectory control. The first involves

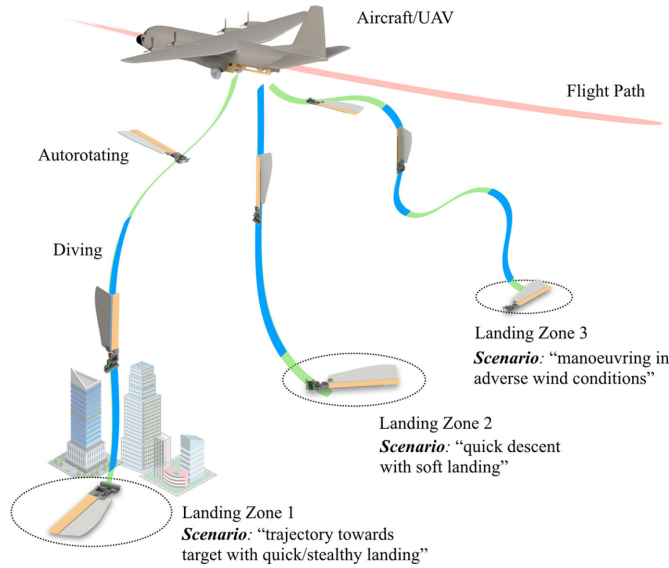


Fig. 1. With the versatility of two flight modes, dSAW is capable of lightweight payload delivery in challenging scenarios. An aircraft or UAV can deploy multiple units of dSAW, which can head toward their target destinations, using autorotating or D-Mode according to mission profile.

changing the pitch of the flap constantly over several rotations in order to induce a precession circle and the craft achieves lateral motion as a result [25]. The second method is once-per-revolution actuation of the pitch of the flap [23],[24], akin to cyclic pitch control of helicopter blades using the swash plate mechanism.

The concept of samara autorotating wing (SAW) has been evolved over several iterations, as described in previous works [26]–[28]. Its most recent version, SAW+[28], is able to enter autorotation quickly regardless of initial launch conditions, and has demonstrated directional control. However, it is easily influenced by tough environmental conditions such as strong gusts of wind. In order to eliminate this weakness, two methods are explored: a new flight mode called the diving mode (D-Mode), and a better glide angle. The latter involves optimizing the design parameters and improving the cyclic control technique for the craft.

When environmental elements are violent, SAW can increase its descent speed significantly by diving, thus being less influenced by lateral wind (see Fig. 2). D-Mode can also be used for a fast and stealthy descent and deployment of payloads. In nature, a number of animals or seeds employ diving as part of the flight. Notably, peregrine falcons [29] use diving (estimated top speed 157 m/s) in order to attack their prey, but losing altitude of up to 60 m when pulling out of the dive. The maple seed, however, performs much better at recovering from a “dive.” A recent research launched maple seeds [30] at 9 m/s and found that they can reach near-zero translational velocity within 150 ms in a rapid deceleration. The maple seed has a much smaller mass than the falcon, yet its rapid deceleration can be attributed more to its ability to convert translational kinetic energy into rotational kinetic energy in a short instant. In UAV research, diving is used as a strategic flight path to land an aquatic UAV on the surface of water [31].

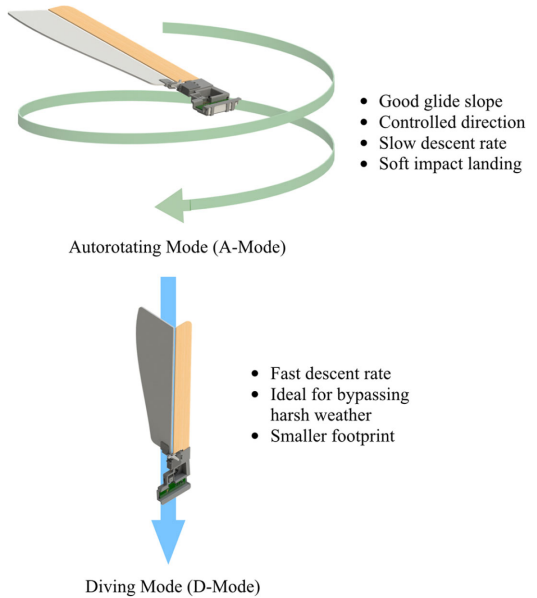


Fig. 2. A-Mode and D-Mode encompass different strengths. These two modes enhance the capability of dSAW, making it suitable for more complex mission profiles and weather conditions.

For any gliding aerial body that has no means for sustained flight, glide angle is a good measure of its effectiveness and range. In mammals, the sugar glider, a nocturnal gliding possum, achieves a gliding angle averaging 29.7° [32] while the northern flying squirrel glides at 26.8° [33]. Flying snakes, although lacking appendages to assist them in their aerial movements, achieve glide angle of 31° late in their flight trajectory [34]. Parafoil canopies may glide up to 11.5° [35]. Interestingly, the glide slope achieved by diving-SAW (dSAW) is close to that of the sugar glider. Although the parafoil may achieve superior glide angles, dSAW’s flight trajectory could be far more complex, due to its ability to dive and decelerate abruptly.

The contributions of this work are as follows.

- 1) A new prototype, named dSAW, is presented. We improved flight dynamics by finding an optimized wing planform and angle of attack of flap for a design configuration that has adequate rotation rate, slow descent rate, and minimum unwanted oscillations. In this work, GA is used to find the optimum solutions.
- 2) A new flight mode (D-Mode) is introduced. dSAW can actively switch between A-Mode and D-Mode, at any part of the descent, achieved by the use of a single actuator on board. This is challenging as a samara-like craft is inclined to autorotate from any possible initial conditions.
- 3) A square cyclic control methodology is introduced. This is an improved control over traditional sinusoidal cyclic control and better suited for direct actuation with a rapid servo. The parameters for this control are also found using GA. This new control methodology, together with the improved design parameters, allows dSAW to achieve a glide angle of 28.9° . To the best of authors’ knowledge, dSAW is the only samara-inspired platform with agility of

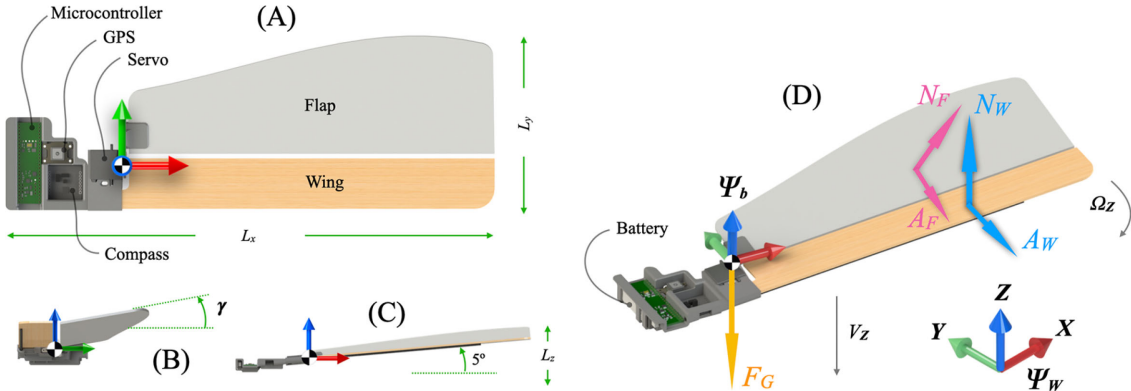


Fig. 3. (a) Top, (b) side, and (c) front views of dSAW design concept. (d) Free body diagram with definitions of world frame Ψ_W (X , Y , Z) and body frame Ψ_b (x , y , z) at the center of gravity. Ω_Z is rotation speed of Ψ_b with respect to Ψ_W and V_Z is the velocity along Z -axis. L_x , L_y , L_z , and mass m of final optimized dSAW are given in Table III. γ is the actuated angle of the flap measured from neutral (horizontal) position. N_W , N_F , A_W , and A_F are normal and axial forces from the wing and the flap, respectively, and F_G is the force due to gravity.

a decent glide slope with directional control, diving, and autorotation modes, achieved using a single actuator.

In this work, we attempt to demonstrate that single-winged autorotating platform can be a capable and exciting contender in the field of micropayload deployment by showing new exciting results and a novel flight mode with highly under actuated control, minimum complexity, and at low cost.

II. DESIGN CONCEPT, DYNAMIC MODEL, AND FLIGHT MODES

SAW prototypes generally consist of a 3D-printed body that houses the electronic components, and a wing laser-cut from thin balsa wood. The on-board electronics include a microcontroller, a three-axis magnetometer, a 5 V step-up voltage regulator, an RC microreceiver, a GPS, a 1-cell lithium-polymer battery, and a servo. The wing is designed such that a straight narrow portion forms the leading edge and a large rear portion forms the flap. The components are strategically placed such that the center of gravity is located very close to the root of the wing.

A. Design Concept

dSAW is developed as the continued effort on SAW+ prototype [28]. SAW+ demonstrated capabilities such as entering autorotation quickly upon launch and achieving directional control during its descent. It was able to achieve a glide angle of 58.4° but when deployed in real-world conditions, it was observed that the trajectory was easily influenced by strong winds. In this work, we look into optimizing its parameters to improve its glide angle and add a new “diving” flight mode. Some changes are made to the choice of the servo, the wing aspect ratio, the component selection, and material choice of wing. Two different attempts were made to improve the glide angle of dSAW.

The first was through increasing its spin rate. By having a higher spin rate, the flap can actuate more frequently, thus providing more aerodynamic force for lateral displacement. During early prototyping and design phase, several attempts were made to increase the spin rate in autorotation. One of the attempts was using blade element theory and GA (similar to the process described in Section III) to find the wing planform, location of

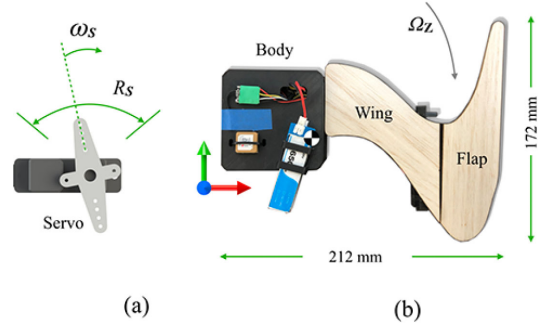


Fig. 4. (a) Definition of servo selection criteria, (b) Top view of a SAW prototype, shaped by GA for fast spin descent.

battery, and servo for higher spin rate. The resulting prototype is shown in Fig. 4(b). It carried identical electronic components as SAW+ except for a larger battery (1 s 650 mAh instead of 1 s 260 mAh). It weighed 88 g, rotated at about 15 Hz, and descended at about 5 m/s. For comparison, SAW+ rotated at 5 Hz, weighed 83 g, and dropped at about 3 m/s. Interestingly, the optimization results placed the servo further outside along the wing, increasing the wing tip mass. Combined with a shorter wing length, it was able to increase the spin rate by a factor of three. To accommodate this, the flap was designed to be the entire outer portion of the wing.

However, it also brought about new challenges. Experiments showed that faster spin rate came with faster descent speed, and it also took longer before it reached its maximum spin rate after being dropped. The other challenge was a need for a very fast actuator, an electronic compass and inertial measurement unit that can cope with the fast rotation. Considering these shortcomings, instead of increasing spin rate of SAW, we chose to focus on an alternative method.

The second way of improving glide angle is by decreasing the descent speed. With a slow descent rate, there is more time to traverse laterally. For slowest descent, reductions in weight can be done while finding an appropriate wing aspect ratio and wing planform. The result is the new concept shown in Fig. 3, and it is the main concept used for this current work. With a

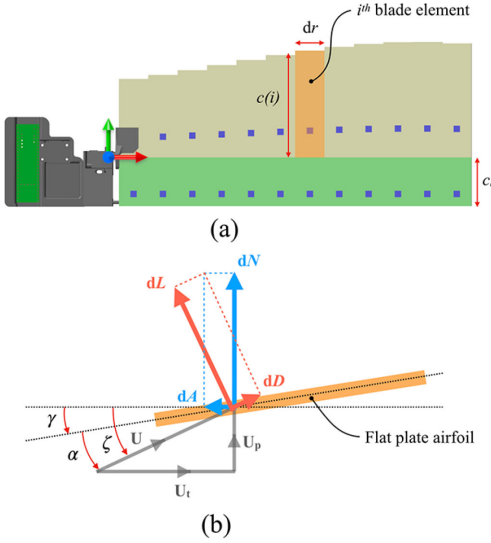


Fig. 5. (a) Visualization of the model in MATLAB Simulink, with definitions of blade element width dr , chord length of blade element $c(i)$ and chord length of the leading edge c_{le} . The small blue squares denote the locations where resolved normal and axial forces are applied back to the model (at the quarter chord). (b) Cross sectional view of the blade element, showing inflow air velocity (U , U_t , U_p), lift, and drag components (dL , dD) and the resolved normal and axial forces (dN , dA).

lighter weight and larger wing span, the prototype is able to enter autorotation almost immediately upon a throw and it possesses a descent rate slow enough for meaningful control and glide angle measurement; this proved to become a suitable model to be tested within the limitations of our test facility.

B. Dynamic Model

The aerodynamic forces acting on its wing and flap can be found using the blade element theory [36]. As it falls, the wing is assumed to be the only component producing useful and significant aerodynamic forces, slicing through clean and undisturbed air. The wing and the flap are each split into n_{be} blade elements, as shown in Fig. 5. The lift and drag forces on each blade element is individually calculated using the following two equations:

$$dL = \frac{1}{2} \rho U^2 c C_l dr, \quad dD = \frac{1}{2} \rho U^2 c C_d dr \quad (1)$$

where dL and dD are the lift and drag forces, respectively, acting on the blade element, ρ is the density of air, U is the relative air velocity interacting with the blade element, c is the chord length of the blade element, C_l and C_d are coefficients of lift and drag, respectively, and dr is the width of the blade element. Since the wing is a flat piece of balsa or foam, flat plate airfoil coefficients are used and they are obtained from NACA Technical Report 3221 [37].

These lift and drag forces are resolved into normal force dN and axial force dA before being applied back into the dynamics simulation using the following equations:

$$dN = dL\cos(\zeta) + dD\sin(\zeta), \quad dA = dL\sin(\zeta) - dD\cos(\zeta) \quad (2)$$

where ζ is the relative inflow angle of the air.

The blade elements are uniformly distributed along the wing and the flap. It is assumed that the aerodynamic forces are acting at the quarter-chord position.

Once the forces from each blade element are computed, the net forces and moments acting on the body about its center of mass can be calculated. As dSAW is rigid body free to rotate and translate in any direction, a standard formulation for equations of motion in 6 degrees-of-freedom (DOF) can be applied [38]. In this work, MATLAB Simscape Multibody is used to develop the dynamic model of dSAW and simulate its various flight dynamics. Simscape Multibody provides a simulation environment for multiple rigid bodies using blocks representing bodies, joints, constraints, force elements, and sensors. 3-D Computer Aided Design drawings assemblies are imported to compute exact masses and moments of inertia and a 3-D animation is generated to visualize the system dynamics. When a 6-DOF joint is used, the standard formulations for equations of motion in 6-DOF are automatically applied. Forces and moments can be specified and applied at component level, such as individual blade elements, and resolved forces and moments are automatically calculated and applied to the rigid body. The Simulink files can be found at¹

C. Flight Modes

1) Autorotation: dSAW in its natural state has mechanical dynamics (such as the dense seed portion, lightweight wing structure, well-defined leading edge) that enables it to enter autorotation easily. However, to help it enter autorotation faster upon any kind of human throw and also to autorotate in the correct direction, the flap is set to a small angle γ_a . This value is found from optimization results described in a following section. Also, the wing is angled upwards 5° along the y -axis of body frame, as shown in Fig. 3(c). These two angles together create the aerodynamic imbalance at the start of the transition into autorotation after a human throw or a dive maneuver.

2) Diving: Diving requires dSAW to alter its mechanical or aerodynamic properties such that it is unable to initiate or remain in autorotation. Normally, this could be achieved in various ways such as altering the CG location or using an additional thruster or aerodynamic surface to deflect the airflow. Such methods require an additional actuator, adding weight, and increasing power drawn from the limited energy stored on-board. We intend to utilize the single actuator that the platform already possesses, for an elegant and simple solution. This means that only the flap is at disposal for any required adjustment. Through multiple experiments, it is found that dSAW is unable to remain in autorotation once the wing stalls, which happens when the flap is actuated to a large angle of attack. Pitching the flap to 90° either up or down (denoted as γ_{d+} or γ_{d-} , respectively) allows the wing to be stalled completely. During a dive, dSAW can accelerate to free-fall speeds.

Fig. 6 shows the range of angles that controls the flight envelope of dSAW, as discussed more in experimental investigations with Fig. 16. When the flap angle is more than the critical flap

¹[Online]. Available: <https://github.com/shanekhw/dSAW>

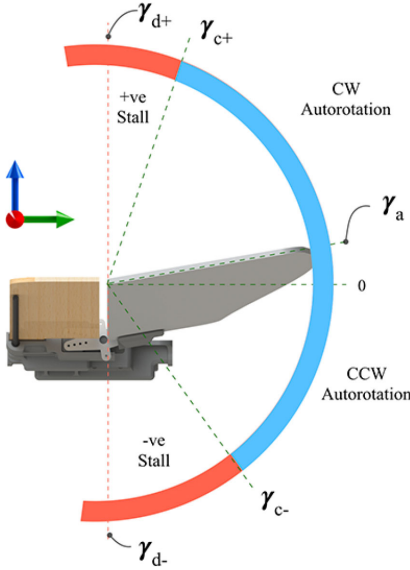


Fig. 6. Definition of flap angles from side view. γ_a is the optimized value of flap angle for A-Mode. γ_{d+} and γ_{d-} are flap angles for D-Mode. γ_{c+} and γ_{c-} are critical flap angles beyond which the wing stalls and dSAW drops faster than V_{max} . These angles are discussed further in the experimental investigation.

angle γ_{c+} and γ_{c-} , which are found to be nonsymmetric about the center, the wing is stalled and the platform begins to dive. Both γ_{d+} and γ_{d-} are flap angles that enable high-speed dive behavior. When the flap angle is in blue region, dSAW generally rotates clockwise (CW) for positive γ or counter-clockwise (CCW) for negative γ . At γ_a , dSAW reaches an optimum autorotation whereby it has a slow and stable descent and it also enters autorotation reliably in the correct direction upon dropping. Hence, this method allows dSAW to transit into dive at any point in the flight and also transit back into autorotation in the correct rotation direction reliably.

III. OPTIMIZATION OF DESIGN PARAMETERS

In various rotary-winged crafts and more prominently on crafts whose entire body rotates during flight (such as the moncopter), there exists a form of precession circle, which is a combined result of gyroscopic precession and aerodynamic forces. This effect is undesirable and it can be observed as oscillations in \mathbf{X} and \mathbf{Y} axes.

In our optimization, we intend to find the wing planform and the flap angle needed to achieve the following objectives:

- 1) minimum drop speed;
- 2) rotation rate of about 6 Hz;
- 3) minimum unwanted oscillations in the \mathbf{X} and \mathbf{Y} axes.

Targeting a 6 Hz rotation speed ensures that it is well within servo actuation speeds and also prevents an unreasonably large wing geometry (slow rotation speed and slow drop speed). The previous prototype, SAW+[28], rotated at 5 Hz. The new prototype is expected to be lighter (due to the removal of certain electronics) while following similar design concept. From preliminary testing, it is found that our simulation tends to overestimate the rotation speed by about 20%. To compensate for this and achieve similar rotation speed as SAW+ in reality,

TABLE I
TABLE OF DESIGN VARIABLES

Parameter	Lower Bound	Upper Bound
C_1	-1	1
C_2	-2	2
C_3	-3	3
C_4	1	100
$dr(\text{mm})$	10	30
$\gamma_a(\text{rad})$	0	0.262

a target of 6 Hz is chosen. Without a target rotation speed, the algorithm may search for a solution at extremely slow rotation at near-stall aerodynamics where our dynamic model may have limited accuracy or extremely fast rotation where the actuator may not be able to keep up.

A. Design Parameters

The wing planform is made up with two components: leading edge and the flap. The leading edge portion of the wing has to attach to a straight carbon rod at the front for structural rigidity and to the flap at the back. This means that the shape of leading edge portion is fully constrained as a rectangle, with a fixed width of $c_{le} = 38$ mm. The flap, therefore, defines the wing planform. The chord lengths of the blade elements of the flap are defined by a polynomial of order 3 to ensure smoothness and to avoid unrealistic changes in chord length. The equation defining flap chord lengths is then arranged as:

$$c(i) = C_1 i^3 + C_2 i^2 + C_3 i + C_4, \quad c_{\min} \leq c(i) \leq c_{\max} \quad (3)$$

where i is the blade element designation ($i \leq n_{be} | i \in \mathbb{Z}^+$), $c(i)$ is the chord length of the respective blade element, and C_1, C_2, C_3 , and C_4 are the coefficients to be determined such that the value of $c(i)$ is bounded between c_{\min} and c_{\max} . Below c_{\min} , the foam flap is not structurally rigid, and above c_{\max} , the overall wing would not fit within the compartment of the C-130 model aircraft, which is described in Section VI-B.

The other design variables are dr , the width of each blade element and γ , flap angle, as shown in the Fig. 5.

B. Formulation

All the design variables can be expressed in a single concatenated vector $\Gamma = [C_1, C_2, C_3, C_4, dr, \gamma_a]^T$, which consists of real numbers except dr , which is integer valued. These design variables can be summarized as per Table I.

The main objective function consists of some subobjective functions: F_1, F_2, F_3 , and F_4 . F_1 is the subobjective function for average rotation speed, which is defined as

$$F_1 = \left(\frac{\sum_{i=n_1}^{n_2} \Omega_Z(t_i)}{n_2 - n_1} - 37.7 \right)^2 \quad (4)$$

where $\Omega_Z(t_i)$ is the angular velocity in the Z -axis at time t_i and 37.7 rad/s is the rotation speed equivalent to 6 Hz. n_1 denotes the step number in the simulation, 3 s from the beginning, and n_2 is the step number at the end of the simulation. The reason for starting at n_1 is to allow some time for the model to settle into autorotation stage. F_2 is the subobjective function for average

drop speed, which is defined as

$$F_2 = -\frac{\sum_{i=n_1}^{n_2} V_Z(t_i)}{n_2 - n_1} \quad (5)$$

where V_Z is the velocity in the Z -axis. Since the craft is traveling downward, V_Z is a negative value. F_3 is the subobjective penalty function for undesired oscillations and is defined as

$$F_3 = \frac{\sum_{i=n_1}^{n_2} (\Omega_X(t_i)^2 + \Omega_Y(t_i)^2)}{n_2 - n_1} \quad (6)$$

where Ω_X and Ω_Y are angular velocities in the X and Y axes, respectively, which represent the body rolls during each rotation. Finally, F_4 is subobjective function for the distance deviation and is defined as

$$F_4 = \sqrt{(d_X(t_s) - d_X(t_f))^2 + (d_Y(t_s) - d_Y(t_f))^2} \quad (7)$$

where d_X and d_Y are distances in X and Y axes with respect to the origin in the world frame. t_s and t_f are start and final times, respectively. This subobjective function serves as another way for penalizing an unstable system whereby it does not oscillate much but it keeps deviating toward a certain direction.

The optimization formulation can be summarized as

$$\Gamma \kappa_1 F_1 + \kappa_2 F_2 + \kappa_3 F_3 + \kappa_4 F_4 \quad (8)$$

where κ_1 , κ_2 , κ_3 , and κ_4 are the weightage coefficients of each subobjective function. Although the optimization problem can be formulated as a multiobjective optimization, it is simplified to produce a single result using a weighted sum from subjective preferences. The coefficients, given in Table III, serve to nondimensionalize the function outputs and bring them to a similar order of magnitude. Highest priority is given to F_2 (lowest drop speed), followed by F_3 (reduce oscillations).

C. Optimization Results

The optimization was run on MATLAB's ga function by simulating the various possible dSAW configurations, using principles of biological evolution and natural selection. It works by using a crossover and mutation function to modify a population of individual solutions in order to obtain the solution with best fitness value. The algorithm is stopped when the best fitness value remains unchanged for 15 consecutive generations. Each simulation is run for 40 s of drop, with a fixed step size of 0.001 s.

The design variables corresponding to the best fitness value is $\Gamma = [-0.0325, 0.4175, 2.1997, 58.5336, 23, 0.1887]^T$. This results in a wing planform shown in both Figs. 3 and 5. When making the actual wing, the smooth shape of the wing is achieved by joining the blade elements together using a spline. The simulation parameters are given in Table III.

IV. SQUARE CYCLIC CONTROL

Cyclic pitch control on helicopter blades is governed by a sinusoidal function such as one given in (10). The blade pitch angle follows a smooth sine curve within a period of one rotor revolution. From a mechanical perspective considering the configuration of the swash plate, such smooth motion is

TABLE II
TABLE OF CONTROL VARIABLES

Parameter	Lower Bound	Upper Bound
γ_o	0	0.175
ϵ	0.01	0.99
γ_{amp}	0	0.175

TABLE III
TABLE OF SIMULATION PARAMETERS

PARAMETERS	
Environment	$\rho_{air} = 1.225 \text{ kg/m}^3$, $g = -9.81 \text{ m/s}^2$
Initial conditions	$V_Z = 0 \text{ m/s}$, $\Omega_Z = -18.8 \text{ rad/s}$
Objective fn coeffs	$\kappa_1 = 100$, $\kappa_2 = 500$, $\kappa_3 = 200$, $\kappa_4 = 1$
Others	$\beta_1 = 1$, $\beta_2 = 10$, $\beta_3 = 400$
	$n_1 = 3000$, $n_2 = 40000$, $t_s = 0 \text{ s}$, $t_f = 40 \text{ s}$
	$n_3 = 10000$, $n_4 = 40000$, $t_{s2} = 10 \text{ s}$, $t_{f2} = 40 \text{ s}$
	$n_{be} = 12$, $c_{min} = 30 \text{ mm}$, $c_{max} = 120 \text{ mm}$
OPTIMIZED DESIGN VARIABLES	
Polynomial coeffs	$C_1 = -0.0325$, $C_2 = 0.4175$, $C_3 = 2.1997$, $C_4 = 58.5336$
Chord lengths (mm)	$c_1 = 61.1$, $c_2 = 64.3$, $c_3 = 68.0$, $c_4 = 71.9$ $c_5 = 75.9$, $c_6 = 79.7$, $c_7 = 83.2$, $c_8 = 86.2$ $c_9 = 88.5$, $c_{10} = 89.8$, $c_{11} = 90.0$, $c_{12} = 88.9$
Radius (mm)	$dr = 23$, $R = 276$
Others	$\gamma_a = 0.1887 \text{ rad}$, $m = 58 \text{ g}$ $L_x = 368 \text{ mm}$, $L_y = 131 \text{ mm}$, $L_z = 44 \text{ mm}$
OPTIMIZED CONTROL VARIABLES	
Control vars	$\gamma_o = 0.1345$, $\epsilon = 0.2010$, $\gamma_{amp} = 0.1188$
Others	$\lambda_c = 0$

logical and desired. Monocopters [23], [24] have also adopted this sinusoidal control strategy. dSAW's flap pitch angle is not mechanically limited by a swash plate, and this allows us to explore other waveforms for its actuation.

We propose to use square waves for cyclic actuation of the flap, as shown in Fig. 7(a). With the proposed control, we would take advantage of the servo's rapid actuation speed, requiring the servo to aggressively switch between maximum, neutral, and minimum actuation angles. Unlike monocopters whose rotation is driven by a thrust unit, dSAW derives its rotational energy from the process of autorotation, which requires the flap angle to be close to its optimum angle γ_a (derived in Section III). The benefit of the proposed square cyclic control is that it allows flap pitch angle to remain close to γ_a [point B in Fig. 7(b)] throughout a major portion of each revolution, and switch to maximum and minimum in the most effective regions. The proposed control scheme can simply be defined as

$$\gamma = \begin{cases} \gamma_o + \gamma_{amp}, & \text{if } \sin(\theta_z + \lambda_c) > \epsilon \\ \gamma_o - \gamma_{amp}, & \text{if } \sin(\theta_z + \lambda_c) < -\epsilon \\ \gamma_o, & \text{otherwise} \end{cases} \quad (9)$$

where γ is the flap pitch angle, γ_o is the offset or neutral point of the cyclic control, γ_{amp} is the cyclic amplitude, θ_z is the current azimuth angle, λ_c is the direction control input from human controller, and ϵ is the threshold that controls the duty cycle θ_d of the square wave. A traditional sinusoidal cyclic control can be defined as

$$\gamma = \gamma_o + \gamma_{amp} \sin(\theta_z + \lambda_c). \quad (10)$$

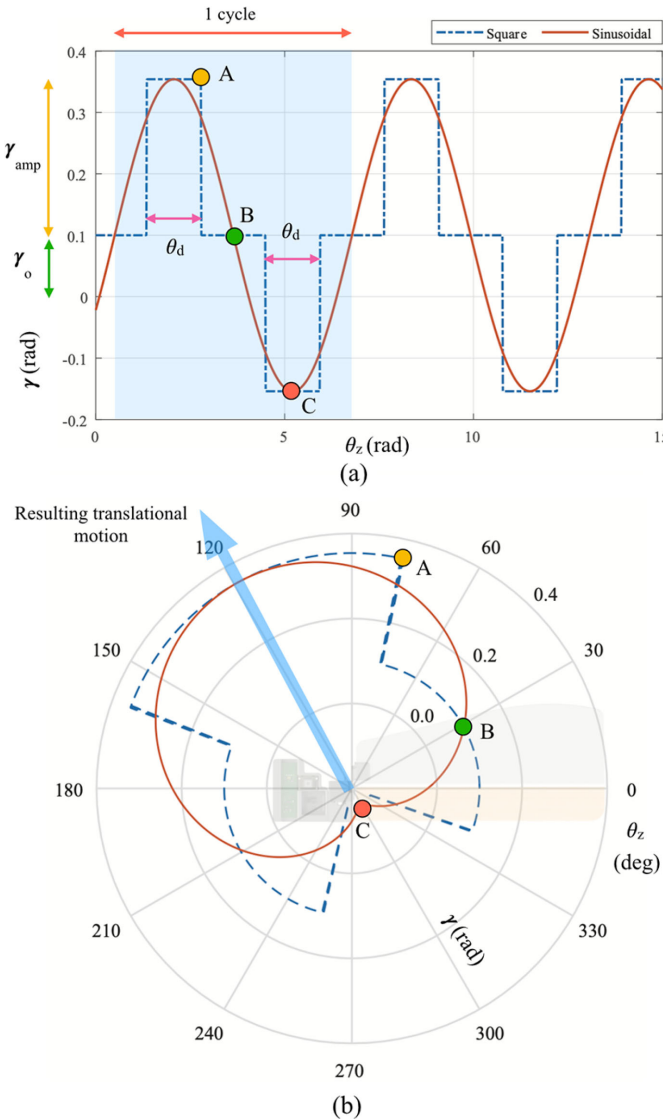


Fig. 7. (a) Proposed square cyclic control compared to traditional sinusoidal cyclic control. (b) Polar plot of flap pitch angle for better visualization of the square cyclic control and sinusoidal control as dSAW's azimuth angle θ_z changes.

In the polar plot shown in Fig. 7(b), the radius of the plot represents the flap pitch angle γ as the craft goes through one complete rotation. In this plot, it is assumed that effects of gyroscopic precession are absent since the craft is rotating at relatively slow speed such as 6 Hz. Therefore, the resulting direction of motion is assumed to be at the center of the region where the flap generates the least lift when it is flapping up.

Next, we find the optimized parameters for the square cyclic control using GA once again. The following describes the formulation briefly.

The control variables are expressed in a single concatenated vector $\Gamma_c = [\gamma_o, \epsilon, \gamma_{\text{amp}}]^T$, which are all real numbers. These variables are bounded between values shown in Table II.

The main objective function also consists of some subobjective functions: G_1 , G_2 , and G_3 . G_1 is the objective function for average rotation speed after control is applied, which can be

defined as

$$G_1 = \left(\frac{\sum_{i=n_3}^{n_4} \Omega_Z(t_i)}{n_4 - n_3} - 44.0 \right)^2 \quad (11)$$

where 44.4 rad/s is the rotation speed at 7 Hz. From our experiments, we found that although γ_a is an angle optimized for stable autorotation, it produces slightly steeper coning angle and rotates too slow for good control. Hence, the target rotation speed during control is increased by 1 Hz. n_3 denotes the step in the simulation when control is first applied and n_4 denotes the end of the simulation. Next is G_2 which is the penalty function for unwanted oscillations after control is applied, which is defined as

$$G_2 = \frac{\sum_{i=n_3}^{n_4} (\Omega_X(t_i)^2 + \Omega_Y(t_i)^2)}{n_4 - n_3}. \quad (12)$$

G_3 is the function for glide angle. Here, we have formulated it such that it is lateral distance traveled over distance dropped. It is a value that should be maximized, hence, assigned as a negative value, which must be minimized

$$G_3 = -\frac{\sqrt{(d_X(t_{s2}) - d_X(t_{f2}))^2 + (d_Y(t_{s2}) - d_Y(t_{f2}))^2}}{\text{abs}(d_Z(t_{s2}) - d_Z(t_{f2}))} \quad (13)$$

where d_Z is the distance along Z -axis with respect to the origin in the world frame. t_{s2} and t_{f2} denote the starting time when control is applied and final time of the simulation, respectively. The combined optimization formulation for control is summarized as

$$\Gamma_c \beta_1 G_1 + \beta_2 G_2 + \beta_3 G_3 \quad (14)$$

where β_1 , β_2 , and β_3 are weightage coefficients of each subobjective function. Similar to design parameter optimization, the weighted sum includes considerations for nondimensionalizing and bringing the subobjectives to similar magnitude, while higher priority is given to G_3 (lower glide angle). The result of this optimization is given in Table III.

V. SIMULATION

In this section, simulation results for autorotation with optimized parameters are given. Comparison between square cyclic control and sinusoidal cyclic control is also shown.

A. Simulation With Optimized Parameters

When building the model for simulation within MATLAB Simulink, the 3D-printed body and electronic components were drawn first in SolidWorks and their basic geometries were imported into MATLAB. The leading edge and the flap are box-shaped geometry with assigned densities. Estimated component masses were assigned to each imported geometry within the Simulink environment where the moment of inertia and the center of gravity were internally calculated.

The dSAW model with optimized design variables Γ has rotation speed $\Omega_Z = -37.6$ rad/s and drop speed $V_Z = -2.06$ m/s. From its given initial condition, dSAW was able to enter stable autorotation within 2 s, with quickly decaying oscillations in Ω_X and Ω_Y , as shown in Fig. 8. The plot shows oscillating values of

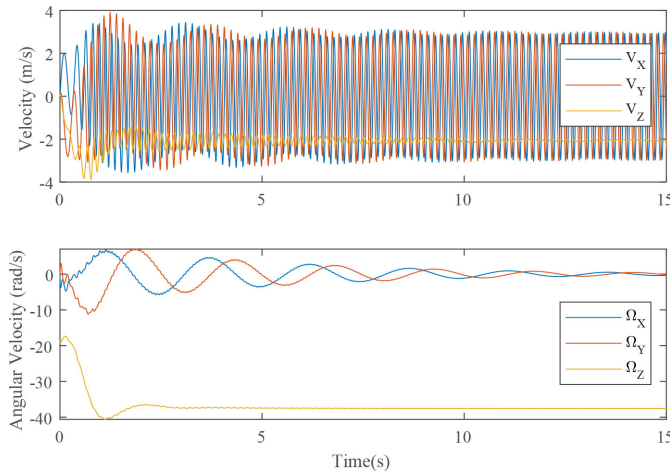


Fig. 8. Simulation results showing linear and angular velocities of dSAW with optimized design variables Γ . It is simulated to be released with initial conditions $V_Z = 0 \text{ m/s}$ and $\Omega_Z = -18.8 \text{ rad/s}$.

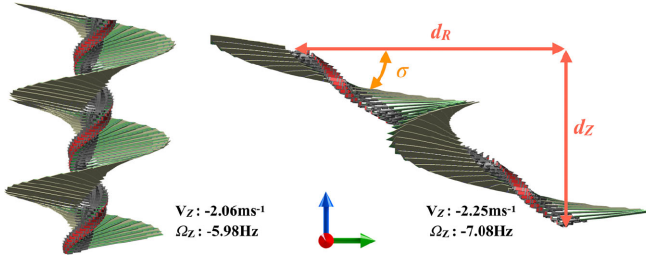


Fig. 9. Autorotation sequence of dSAW model in simulation for normal autorotation (left) and direction controlled autorotation (right). Each frame is captured 0.005 s apart. The definition of glide angle σ is also shown.

V_X and V_Y due to the body frame not being placed at the center of rotation.

B. Simulation of Control

The optimized values of γ_o , ϵ , and γ_{amp} were used for the proposed square cyclic control described in (9), which was applied to the model at simulation time $t_{s2} = 10 \text{ s}$. The same γ_o and γ_{amp} were used for the traditional sinusoidal cyclic control described in (10), starting at the same time $t_{s2} = 10 \text{ s}$. The two resulting trajectories are shown in Fig. 10 for comparison. Glide angle σ (as shown in Fig. 9) is defined by $\sigma = \tan^{-1} \frac{d_Z}{d_R}$ where d_Z is the vertical distance dropped and d_R is the horizontal distance traveled. It can be seen that the proposed control scheme produced a better glide angle and traveled a further distance within the same simulated period. Decaying oscillations can be observed on Ω_Z , V_Z , and V_R plots (with bigger oscillations for square cyclic control). Increasing γ_{amp} beyond its optimum value results in disruption of autorotation of the platform in both simulation and experiments. This indicates that the optimum parameters were pushing the platform to its maximum capability, close to making it unstable. Fig. 10 shows a comparison between various translational and angular velocities of the two controls. It can be seen that square cyclic control created oscillations of higher amplitude, but it had higher average Ω_Z and horizontal

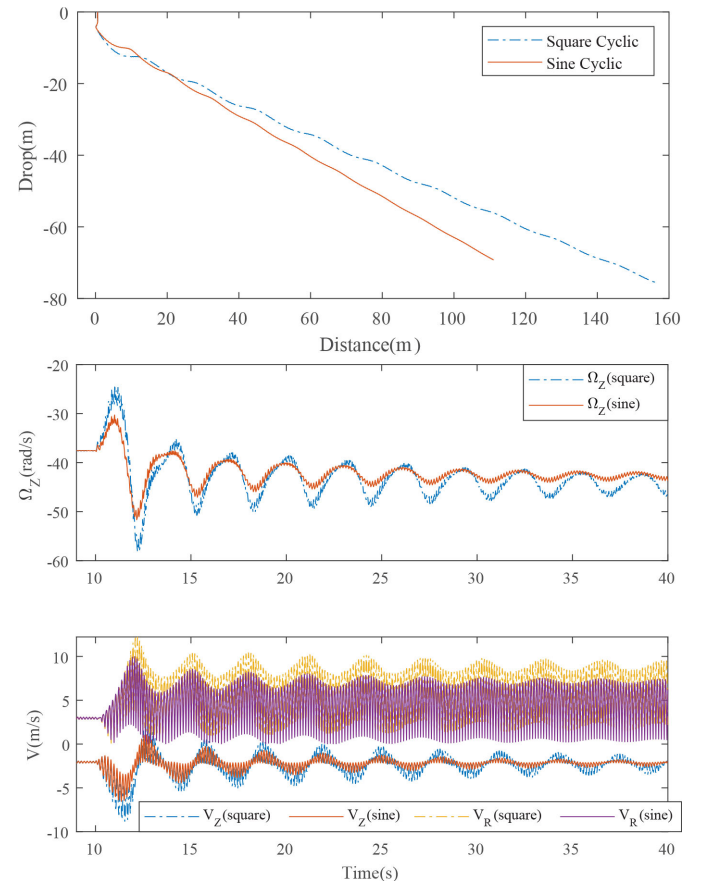


Fig. 10. Comparison of drop trajectory, Ω_Z , V_Z , and V_R (9 s to 40 s) under square cyclic and sinusoidal cyclic control, applied 10 s after dSAW is simulated to drop. Glide angle of square cyclic is 0.4716 rad (27.0°) and that of sine cyclic is 0.6086 rad (34.9°).

velocity V_R while having similar drop speed V_Z to sinusoidal cyclic control.

VI. EXPERIMENTAL INVESTIGATION

The following two types of experiments were conducted: a) semoutdoor drop from 30 m and b) outdoor deployments from fixed-wing UAV. The purpose of the semoutdoor experiments is to repeatedly test control maneuvers in A-Mode in low wind condition and user-commanded transitions between A-Mode and D-Mode. Outdoor deployments from fixed-wing UAV demonstrate the use case of dSAW in real-life missions.

A. dSAW Prototype

When building the dSAW prototype, we started with the selection of its single actuator. We found multiple servos that were available and made a comparison in Table IV. In order to obtain a good glide angle and agile motion such as diving, a servo [see Fig. 4(a)] needs to have a) a good range of actuation R_s , b) fast actuation speed ω_s and c) light weight m_s . The criteria may be summarized as a selection nondimensional score S , which can be defined as

$$S = S_1(R_s - \Theta_1) + S_2(\omega_s - \Theta_2) + S_3(\Theta_3 - m_s) \quad (15)$$

TABLE IV
SERVO COMPARISON

	Range (R_s) (degrees)	Speed (ω_s) (deg/s) @4.8V	Weight (m_s) (grams)	S
BA D03013	125 (Θ_1)	857 (Θ_2)	3.0 (Θ_3)	0
MKS DS480	149	882	9.5	4.4
MKS DS95i	115	1277	21.2	0.4
HK-5330	112	1200	1.9	0.9
$\Theta = 135^\circ, S_1 = 0.2, S_2 = 0.01, S_3 = 0.1$				

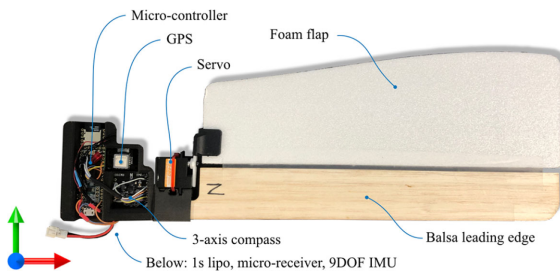


Fig. 11. dSAW prototype “N.”

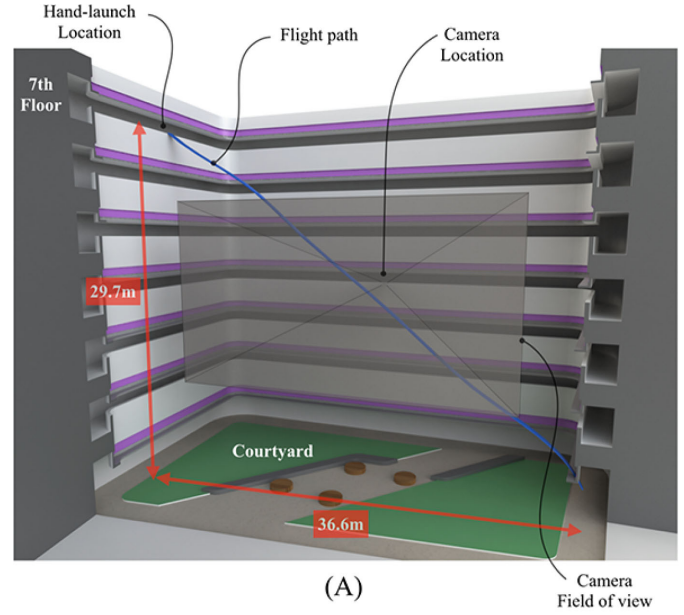
where S_1 , S_2 , and S_3 are coefficients, selected such that all variables have the same order of magnitude, identified in Table IV. BA D03013 was previously used for SAW+ and is used as a reference servo for our comparison. Coefficient S_1 is set slightly higher because for dSAW to enter D-Mode, having a high R_s is considered most important. MKS DS480 scored the highest S and is used on our dSAW prototypes.

The dSAW prototype, shown in Fig. 11, consists of a seed-like portion, which is a 3D-printed part (Markforged Onyx). It houses a microcontroller (Teensy 3.5), a three-axis magnetometer (PNIRM3100), a GPS (OriginGPS ORG1510), a 9DOF IMU (EM7180 SENtral), a microreceiver (FrSky), a 5 V regulator (Pololu), a 1 s 260 mAh lithium-polymer battery (BetaFPV), and a servo (MKS DS480). The leading edge portion of the wing (laser-cut 2.5 mm balsa) is slotted in and attached using wing tape to a 2.5 mm carbon rod, which extends from the seed portion. The flap (laser-cut 2.5 mm foam) is attached to the leading edge using wing tape and is also held in place by the servo horn attachment. Overall, the prototype weighs just 58 g, which is 34% lighter than the previous generation SAW+ [28]. The weight savings are achieved by the absence of Pixracer and its GPS (which was only used for logging IMU data and GPS data) and the use of lighter material for flap.

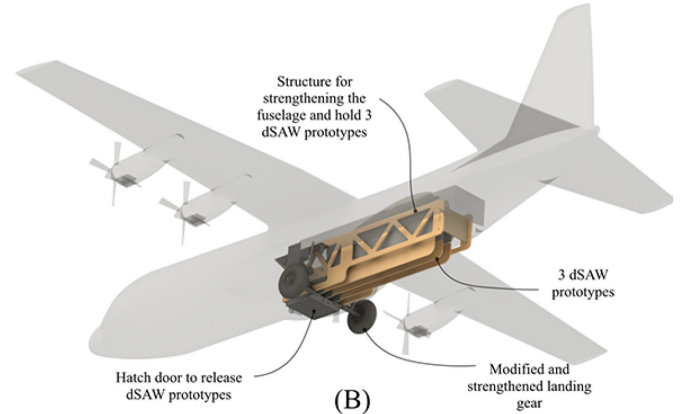
Three similar prototypes were made with this design and are named as “M,” “N,” and “P.”

B. Experiment Setup

The semi-indoor drop tests involved hand throwing or launching of dSAW prototypes from the seventh floor of SUTD Building 2 toward the courtyard on the ground floor, as shown in Fig. 12(a). This is about 30 m of drop height. On the fourth floor, a Nikon P1000 camera was placed on a tripod to take high quality zoomed-in pictures of dSAW to record its minimum glide angle and the flight transitions in subsequent experiments.



(A)



(B)

Fig. 12. (a) Depiction of the semi-indoor experiment setup. dSAW prototypes were dropped from seventh floor toward the courtyard on first floor. Since the building surrounds the whole drop region, wind is assumed to be absent. A camera captured the flight path from an orthogonal view. (b) Model aircraft C130 was modified to carry and deploy three dSAW prototypes.

Because the experiment setup was semi-indoors, GPS coverage was minimum.

For the outdoor deployment, a model aircraft (Avios C-130) was modified as a carrier aircraft. It has a length of 1195 mm, a wingspan of 1600 mm and a take-off weight of about 2400 g. It uses four 1000 kV brushless motors for its propulsion. Its fuselage is just wide enough to house three dSAW prototypes and a release mechanism. The aircraft’s fuselage was cut open and a new structure to hold and release dSAW prototypes was added, as shown in Fig 12(b). The model aircraft’s original retractable landing gear mechanism and operational hatch door were removed to save weight. A Pixracer with PX4 firmware was installed on the aircraft to aid with flight controls. The aircraft was always flown manually in our experiments.

C. Semioutdoor Drop From 30 m

Three different experiments were conducted for semioutdoor drop within the university campus.

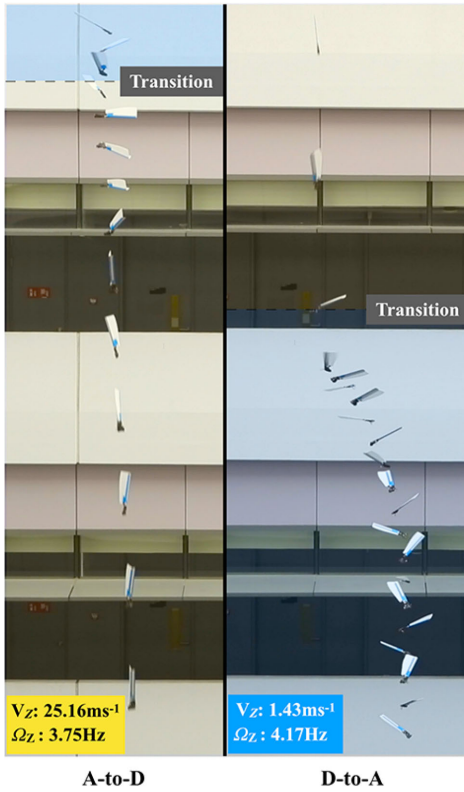


Fig. 13. Two transitions for negative stall (γ_{d-} used for D-Mode). Each frame was captured 0.1 s apart.

1) Transition Between Modes: The transitions between flight modes (A-Mode and D-Mode) described in Section II-C were tested and observed. The flap angle was manually commanded to switch from γ_a to γ_{d-} (negative stall) or γ_{d+} (positive stall) and back to γ_a within the 30 m drop. The resulting transitions were captured from Nikon P1000 camera with zoom applied, as shown in Fig. 13. The notable parameters for these transitions for both cases are plotted in Fig. 14 where the highlighted region for D-Mode is defined with respect to flap angle γ . It was observed that for A-to-D transition, the change was almost instantaneous and dSAW achieved its dive pose in just half a rotation ($t_{AD1} = 250$ ms) for negative stall. For positive stall, the transition was slightly more gentle and took slightly longer ($t_{AD2} = 355$ ms). The flight path remained relatively vertical for both A-to-D transitions. For D-to-A transition, the delay was usually slightly longer ($t_{DA1} = 341$ ms and $t_{DA2} = 950$ ms). t_{DA2} was recorded to be higher, but D-to-A transitions for either case may vary in duration depending on environmental conditions. The delay in D-to-A transition exhibits itself also in the altitude plots in both Figs. 14 and 20, where altitude was still decreasing rapidly after the transition was triggered. This indicates that dSAW had not reached its terminal velocity during its dive in all our tests. It should also be noted that the barometer was updating every 500 ms making the delay effect more pronounced.

At the instance of D-to-A transition, dSAW spun very fast (12.35 Hz) and experienced peak acceleration in x and y axes due to large centrifugal forces at the location of the IMU.

The values peak beyond 8 g for a short period. The maximum range for the accelerometer and gyroscope are 8 g and 2000°/s, respectively, in each axis.

2) Glide Angle Measurement: The dSAW prototype was launched using a hand motion intended to assist entering autorotation immediately. This involved holding the prototype from above its center of gravity and giving it a CW rotation while releasing it. The intention was to let it enter its full autorotation before much height was lost.

Once it was in full autorotation, a manual *RC* command triggered the square cyclic control, from (9) using optimized parameters, to steer dSAW in a direction orthogonal to the camera. From about 15 m above ground, a Nikon P1000 camera captured a video of its trajectory. From the video, frames were extracted and the glide angle of dSAW was measured visually. The average glide angle was 0.5044 rad (28.9°), as shown in Fig. 15. During cyclic flap actuation, dSAW rotated at 4.46 Hz and dropped at about 1.04 m/s.

Similar experiments were conducted with sinusoidal cyclic control using the same parameters. An average glide angle of about 0.6817 rad (39.1°) was obtained. The square cyclic control was seen to perform better than the sinusoidal cyclic control in both the simulation and the experiment.

3) Flight Envelope: To investigate flight behavior of dSAW for different range of flap angles described in Fig. 6, the prototype was dropped repeatedly from 30 m with each time γ set to angles from -90° to 90° , at intervals of 10° . This experiment was repeated 3 times and the average values of final rotation speed Ω_Z and drop speed V_Z were recorded. The values are plotted in Fig. 16. dSAW tends to rotate CW for $+\gamma$ and CCW for $-\gamma$. However, for $-10^\circ < \gamma < 10^\circ$, the direction of rotation became less certain as it was more likely to be influenced by factors such as initial conditions, hand launch variations, or gusts of wind.

From the graph, we can observe that the flight dynamics of dSAW are not very symmetric about positive and negative γ values. This is expected since the design of dSAW is not symmetric. V_Z values tend to increase aggressively on negative γ . We can also observe that V_Z value is smallest at around $\gamma = 10^\circ$, aligning with γ_a from our optimized result. It should be noted that we could not measure the steady state V_Z and Ω_Z for $\gamma = \pm 90$ within the drop height of 30 m.

We define the maximum drop velocity for autorotation, V_{\max} , to be -5 m/s, as it can be seen that V_Z values increase sharply after this point. dSAW can be considered stalling when V_Z is beyond V_{\max} as its wing is unable to produce useful aerodynamic forces. Hence, the critical flap angles are $\gamma_{c-} = -60^\circ$ and $\gamma_{c+} = 70^\circ$.

As the R_s of the servo is 149°, the flap actuation region of dSAW was set at $-90^\circ < \gamma < 59^\circ$, taking advantage of aggressive diving speeds for large negative γ values while cyclic actuation happens at small positive γ values.

It was observed that dSAW with the flap at γ_a rotated at about 4.17 Hz and dropped at about 1.43 m/s. With flap set at γ_{d+} , the fastest drop speed measured during outdoor experiments was 25.16 m/s, which is 17.6 times A-Mode's drop speed. However, this measured speed is not yet its steady-state dive

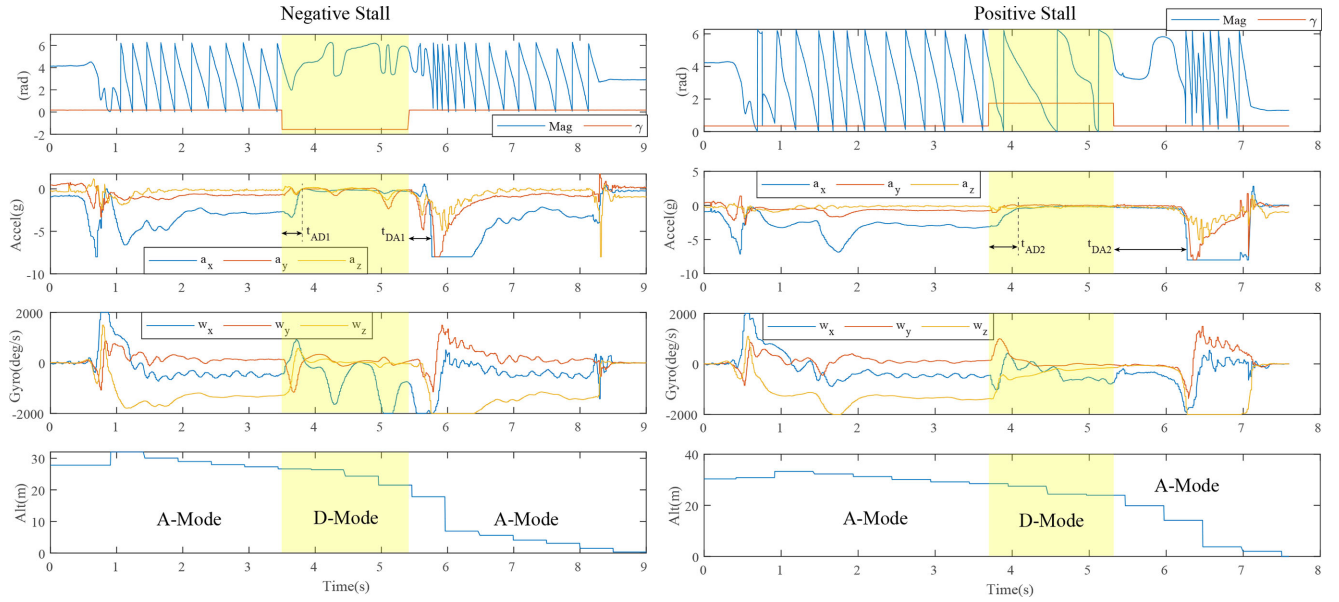


Fig. 14. Magnetometer, accelerometer, gyroscope, and barometer data for transition from A-Mode to D-Mode (negative stall and positive stall), then back to A-Mode within 30 m drop. $t_{AD1} = 250$ ms, $t_{DA1} = 341$ ms, $t_{AD2} = 355$ ms, $t_{DA2} = 950$ ms.



Fig. 15. dSAW prototypes were dropped by hand and square cyclic control was applied shortly after. Still frames of dSAW were extracted and displayed in sequence to show its pose. An average glide angle 0.5044 rad (28.9°) was achieved. Lower right corner shows a close up of Drop 3. Each frame was captured 0.25 s apart, hence, dSAW had rotated slightly more than 1 rotation between each frame.

speed (terminal velocity), which we were unable to obtain due to height limitations of UAV flight.

D. Outdoor Deployments From Fixed-Wing UAV

The purpose of this experiment was to simulate real-life deployment of dSAW prototypes. In an actual deployment, dSAW may be carried by a multirotor or fixed-wing UAV or even an actual aircraft. In this experiment, a modified C-130 model aircraft was used to deploy the prototypes.

The aircraft was flown in a straight line, at about 100 m above ground level with a horizontal speed of around 72 km/h. The hatch-door was triggered to open, releasing all three dSAW prototypes (named M , N , and P) at the same time as shown in Fig. 17. After release, all prototypes entered autorotation almost immediately, due to the flap angles being set at γ_a . About 10 s later, a command signal was sent to all dSAWs simultaneously, using on-board radio. With this command, N was tasked to travel West, M to North, and P to East, visually forming a T-shape in the sky. On-board GPS data are plotted and

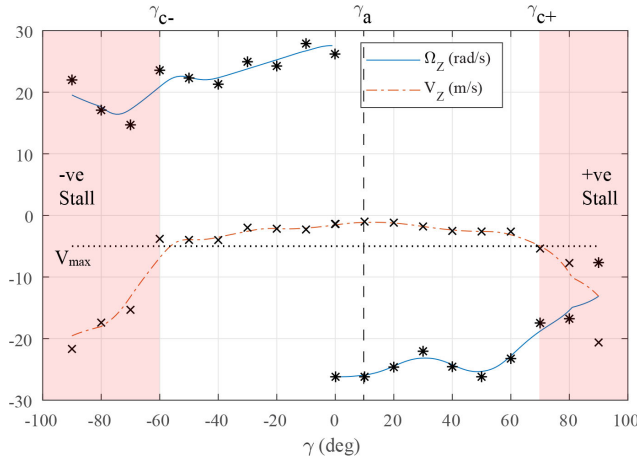


Fig. 16. Flight envelope of dSAW, and the definition of the stall region.

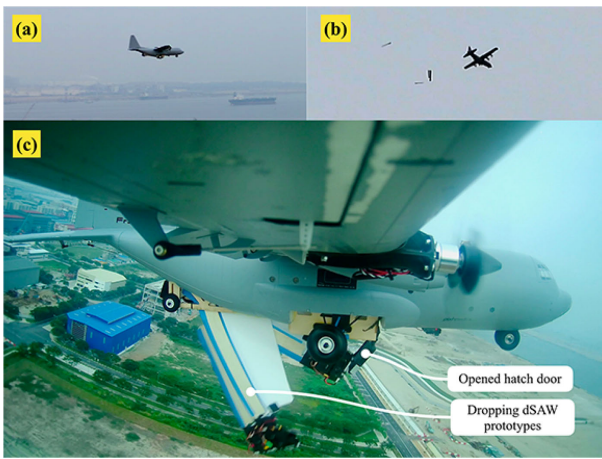


Fig. 17. (a) Aerial camera view of model aircraft C-130 flying to deploy dSAW prototypes, (b) ground camera view shortly after the release of 3 dSAW prototypes from C-130, (c) wing camera view of the moment of drop, when the hatch door was triggered to open, releasing 3 dSAW prototypes simultaneously.

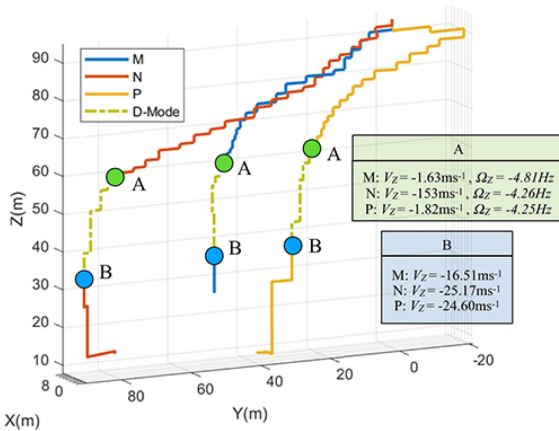


Fig. 18. Flight trajectories of dSAW prototypes M , N , and P as recorded by their on-board GPS. Values of V_Z and Ω_Z before A-to-D transition and V_Z before D-to-A transition are given.

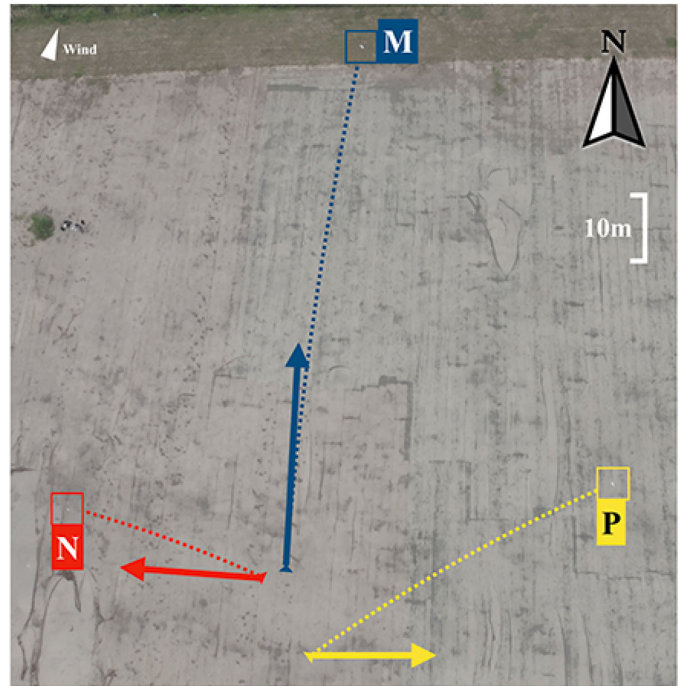


Fig. 19. Aerial picture showing the estimated flight trajectories of dSAW prototypes M , N , and P and their commanded cyclic control directions, before entering dive. Attached supplementary video can also be seen at <https://youtu.be/h1UJhhoAxVw>.

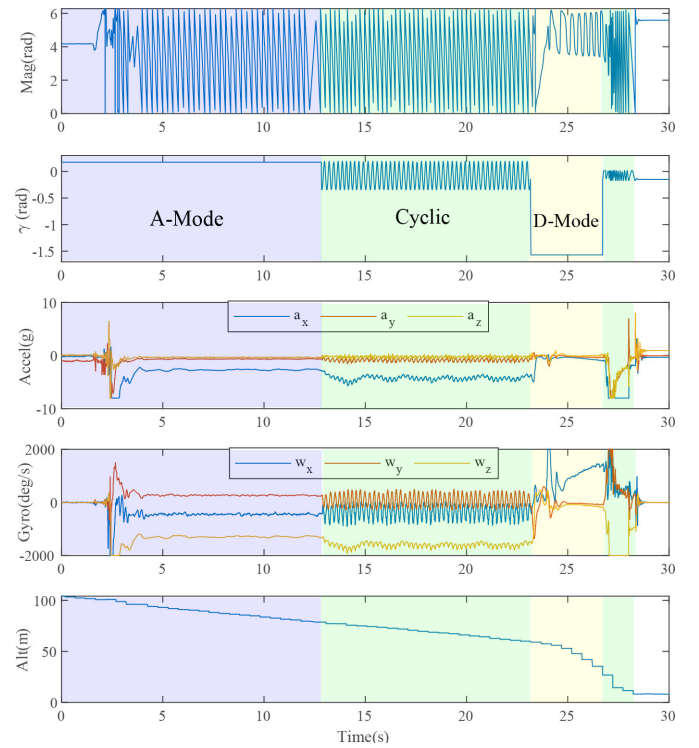


Fig. 20. Data from magnetometer, γ values and IMU of dSAW “ P ” after it was launched from C-130.

shown in Fig. 18. Aerial and ground videos were recorded, which showed the flight trajectory visibly. A snapshot from an aerial camera is shown in Fig. 19, where estimated flight trajectories and its deviation from intended flight path are shown. A mild and steady wind was present during the experiment, which accounted for the deviations in trajectory. All prototypes were programmed to enter D-Mode as soon as the on-board barometer registered about 50 m above ground. Diving to quickly approach the ground, the prototypes entered A-Mode automatically again once 18 m above ground level, to slow down their descent for a safe landing.

The data collected from model P is shown in Fig. 20, as an example. It shows stages of A-Mode, cyclic control, D-Mode and finally back to A-Mode with smaller cyclic signals. From the graphs, it is observed that upon cyclic control, dSAW spun slightly faster and it had small oscillations in its body frame ω_x and ω_y , indicating that the tip path plane was tilted.

VII. DISCUSSION AND FUTURE WORK

It can be observed that the simulation and experimental drop speeds V_Z and rotation speeds Ω_Z are not very close. However, the ratio $\frac{V_Z}{\Omega_Z}$ is similar as it is 0.344 for simulation and 0.343 for experiment. The use of the blade element theory has its limitation and assumptions, but it is good enough to predict reasonably accurate model dynamics in steady state. Using GA on this dynamic model with specific objectives, we find an optimized wing planform that achieves slower descent speed than predicted in simulation. It was visually observed during the experiments that the abrupt and aggressive movements of the flap in square cyclic control partially acted similar to a flapping wing, creating transient aerodynamics forces. These forces were observed to act in favor of improving the glide angle, making dSAW a more agile platform. As opposed to sinusoidal cyclic control, square cyclic control engages the flap at up, down or neutral positions, allowing the craft to increase or decrease lift at exact periods during a cycle of rotation. The upward or downward stroke of the flap tends to slow down the rotation speed, while the neutral angle enables the craft to regenerate the lost speed. Actuation angles that are too large tend to destabilize the autorotation process.

For a rotary wing that lacks any form of on-board propulsion, a glide angle of 28.9° is a notable achievement and the first of its kind in a documented work. A fixed-wing type platform may easily achieve similar or better glide angles with simpler, well-explored control methodology. Flight by autorotation, on the other hand, is inherently nonlinear, which requires novel nonlinear control strategies for the increased performance. Compared to fixed wing platforms, which tumbles upon release with nonideal initial conditions, dSAW can quickly enter autorotation, maximizing its useful flight envelope. Additionally, D-Mode adds value for various mission profiles where stealth and speed are critical factors. The platform, in A-Mode, may still be vulnerable to rough winds, but D-Mode allows it to skip quickly through tough environmental conditions. The authors believe that this is the first research for an autorotating craft to

have bidirectional flight transition and to have trajectory control by using only one actuator.

The glide angle is optimized with limited number of design and control variables and while the use of GA does not guarantee global optimum, it is less likely to be stuck in a local optimum. In order to improve its glide angle even further, new approaches might be needed. Our future work includes new design explorations by adding a small propulsion to increase lift, therefore reducing descent speed, to increase lateral distance traveled.

A drawback of the current platform is that it is unable to carry heavy loads without considerably increasing its size. A study could be done to evaluate the scalability of the platform. In its current form, dSAW is suitable to carry microsensors (not more than 15 g) for data collection.

Other future work includes integrating the on-board electronic components into a compact custom printed circuit board, which can then act as a multifunctional structure. This will save weight, reduce clutter, and simplify the manufacturing process of dSAW. Ultimately, development on the software could be done to make dSAW a fully autonomous GPS-guided platform, adding sensors for it to intelligently decide and switch between A-Mode and D-Mode while planning its trajectory.

ACKNOWLEDGMENT

The authors would like to thank to A. Kapoor who assisted with facilitating many outdoor drop tests.

REFERENCES

- [1] A. D. Kahn and D. J. Edwards, "Navigation, guidance, and control of a micro unmanned aerial glider," *J. Guid., Control, Dyn.*, vol. 42, pp. 1–11, 2019.
- [2] A. M. Brindejonc, "Design and testing of an autorotative payload delivery system: The autobody," Ph.D. dissertation, Department of Aerospace Engineering, University of Maryland, College Park, MD, USA, 2005.
- [3] P. Corke, S. Hrabar, R. Peterson, D. Rus, S. Saripalli, and G. Sukhatme, "Deployment and connectivity repair of a sensor net with a flying robot," in *Proc. 9th Int. Symp. Exp. Robot. IX*, 2006, pp. 333–343.
- [4] W.-Z. Song, R. Huang, M. Xu, A. Ma, B. Shirazi, and R. LaHusen, "Air-dropped sensor network for real-time high-fidelity volcano monitoring," in *Proc. 7th Int. Conf. Mobile Syst., Appl., Services*, 2009, pp. 305–318.
- [5] R. Benney, J. Barber, J. McGrath, J. McHugh, G. Noetscher, and S. Tavan, "The new military applications of precision airdrop systems," in *Proc. Infotech, Aerosp.*, 2005, pp. 2005–7069.
- [6] R. Benney, A. Meloni, A. Cronk, and R. Tiaden, "Precision airdrop technology conference and demonstration 2007," in *Proc. 20th AIAA Aerodyn. Decelerator Syst. Technol. Conf. Seminar*, 2009, pp. 2009–2927.
- [7] R. J. Wood, "The first takeoff of a biologically inspired at-scale robotic insect," *IEEE Trans. Robot.*, vol. 24, no. 2, pp. 341–347, Apr. 2008.
- [8] A. A. Paranjape, S.-J. Chung, and J. Kim, "Novel dihedral-based control of flapping-wing aircraft with application to perching," *IEEE Trans. Robot.*, vol. 29, no. 5, pp. 1071–1084, Oct. 2013.
- [9] R. V. Kulkarni and G. K. Venayagamoorthy, "Bio-inspired algorithms for autonomous deployment and localization of sensor nodes," *IEEE Trans. Systems, Man, Cybern., Part C (Appl. Rev.)*, vol. 40, no. 6, pp. 663–675, Nov. 2010.
- [10] M. Mitchell, *An Introduction to Genetic Algorithms*. Cambridge, MA, USA: MIT Press, 1998.
- [11] K. Varshney, S. Chang, and Z. J. Wang, "The kinematics of falling maple seeds and the initial transition to a helical motion," *Nonlinearity*, vol. 25, no. 1, pp. C1–C8, 2011.
- [12] K. Yasuda and A. Azuma, "The autorotation boundary in the flight of samaras," *J. Theor. Biol.*, vol. 185, no. 3, pp. 313–320, 1997.
- [13] E.-J. Lee and S.-J. Lee, "Effect of initial attitude on autorotation flight of maple samaras (*acer palmatum*)," *J. Mech. Sci. Technol.*, vol. 30, no. 2, pp. 741–747, 2016.

- [14] A. Kellas, "The guided samara: Design and development of a controllable single-bladed autorotating vehicle," Master's thesis, Department of Aeronautics and Astronautics, Massachusetts Institute of Technology, Cambridge, MA, USA, 2007.
- [15] P. E. Pounds and S. P. Singh, "Integrated electro-aeromechanical structures for low-cost, self-deploying environment sensors and disposable UAVs," in *Proc. IEEE Int. Conf. Robot. Autom.*, 2013, pp. 4459–4466.
- [16] J. Mitchell and J. A. Marshall, *Design of a Novel Auto-Rotating UAV Platform for Underground Mine Cavity Surveying*, Adaptive Technology Centre, Queen's Univ., Kingston, ON, USA, 2017.
- [17] B. T. Flood, "Development and analysis of an autorotating, disposable micro air vehicle for tactical surveillance," *UNSW Canberra at ADFA J. Undergraduate Eng. Res.*, vol. 7, no. 2, pp. 1–20, 2015.
- [18] I. Kroo, "Single-winged autorotating brake for sensor deployment on mars," NASA, Washington, DC, USA, Rep. NCC 2–5058, 1995.
- [19] P. Pounds, T. Potie, F. Kendoul, S. Singh, R. Jurdak, and J. Roberts, "Automatic distribution of disposable self-deploying sensor modules," in *Experimental Robotics*. Berlin, Germany: Springer, 2016, pp. 535–543.
- [20] A. Kahn and D. Edwards, "Navigation, guidance and control for the cicada expendable micro air vehicle," in *Proc. AIAA Guid., Navigat., Control Conf.*, 2012, pp. 2012–4536.
- [21] P. Ifju, D. Jenkins, S. Ettinger, Y. Lian, W. Shyy, and M. Waszak, "Flexible-wing-based micro air vehicles," in *Proc. 40th AIAA Aerosp. Sci. Meeting Exhibit.*, 2002, pp. 2002–0705.
- [22] *Project Perdix*, 2011. [Online]. Available: <https://beaverworks.ll.mit.edu/CMS/bw/projectperdixcapstone>
- [23] J. Houghton and W. Hoburg, "Fly-by-wire control of a moncopter," Massachusetts Institute of Technology, Cambridge, MA, USA, Project Rep. 16.622, 2008.
- [24] K. Fregene and C. L. Bolden, "Dynamics and control of a biomimetic single-wing nano air vehicle," in *Proc. Amer. Control Conf.*, 2010, pp. 51–56.
- [25] D. J. Pines, J. S. Humbert, J. E. Hubbard, E. R. Ulrich, I. Faruque, and J. Grauer, "Control model for robotic samara: Dynamics about a coordinated helical turn," *J. Guid., Control, Dyn.*, vol. 33, no. 6, pp. 1921–1927, 2010.
- [26] S. K. H. Win *et al.*, "Direction controlled descent of Samara Autorotating Wings (SAW) with n-wings*," in *Proc. IEEE Int. Conf. Robot. Autom.*, 2018, pp. 6553–6559.
- [27] S. K. H. Win, L. S. T. Win, G. S. Soh, and S. Foong, "Design, modelling and control of collaborative samara autorotating wings (SAW)," *Int. J. Intell. Robot. Appl.*, 2019, pp. 1–14.
- [28] S. K. H. Win, L. S. T. Win, D. Sufiyan, G. S. Soh, and S. Foong, "Dynamics and control of a collaborative and separating descent of samara autorotating wings," *IEEE Robot. Autom. Lett.*, vol. 4, no. 3, pp. 3067–3074, Jul. 2019.
- [29] V. A. Tucker, "Gliding flight: Speed and acceleration of ideal falcons during diving and pull out," *J. Exp. Biol.*, vol. 201, no. 3, pp. 403–414, 1998.
- [30] V. M. Ortega-Jimenez, N. S.-W. Kim, and R. Dudley, "Superb autorotator: Rapid decelerations in impulsively launched samaras," *J. Roy. Soc. Interface*, vol. 16, no. 150, 2019, Art. no. 20180456.
- [31] R.-A. Pelouquin, D. Thibault, and A. L. Desbiens, "Design of a passive vertical takeoff and landing aquatic UAV," *IEEE Robot. Autom. Lett.*, vol. 2, no. 2, pp. 381–388, Apr. 2017.
- [32] S. M. Jackson, "Glide angle in the genus petaurus and a review of gliding in mammals," *Mammal Rev.*, vol. 30, no. 1, pp. 9–30, 2000.
- [33] K. Vernes, "Gliding performance of the northern flying squirrel (glaucomys sabrinus) in mature mixed forest of eastern canada," *J. Mammal.*, vol. 82, no. 4, pp. 1026–1033, 2001.
- [34] J. J. Socha, "Kinematics: Gliding flight in the paradise tree snake," *Nature*, vol. 418, no. 6898, p. 603, 2002.
- [35] M. Ward, A. Gavrilovski, and M. Costello, "Glide slope control authority for parafoil canopies with variable incidence angle," *J. Aircr.*, vol. 50, no. 5, pp. 1504–1513, 2013.
- [36] G. J. Leishman, *Principles of Helicopter Aerodynamics*. Cambridge, U.K.: Cambridge Univ. Press, 2006.
- [37] B. H. Wick, "Study of the subsonic forces and moments on an inclined plate of infinite span," Neighborhood Assistance Corporation of America, Boston, MA, USA, Rep. TN-3221, 1954.
- [38] P. C. Hughes, *Spacecraft Attitude Dynamics*. Chelmsford, MA, USA: Courier Corporation, 2012.



Shane Kyi Hla Win received the B.E. and Ph.D. degrees in mechanical engineering from the Singapore University of Technology and Design (SUTD), Singapore, 2015 and 2020, respectively.

He is currently with the Temasek Laboratories @ SUTD as a Postdoctoral Research Fellow. His research interests include nature-inspired UAVs, optimization of design parameters, flight dynamics, and flight control of UAVs. His current research involves optimizing the design and modeling Samara Autorotating Wings (SAW) for lightweight payload delivery and Single Actuator Monocopter (SAM).



Luke Soe Thura Win received the B.E. degree in electrical and electronics engineering from Nanyang Technological University, Singapore, in 2014.

His research interests include unconventional UAV design and development, such as Transformable HOvering Rotorcraft (THOR), Samara Autorotating Wings (SAW), and Single Actuator Monocopter (SAM).



Danial Sufiyan received the B.Eng. degree in engineering product development from the Singapore University of Technology and Design (SUTD), Singapore, in 2016. He is currently working toward the Ph.D. degree in engineering product development with SUTD.

His research interests include unconventional and nature-inspired unmanned aerial vehicles (UAVs), control, simulation and visualization, as well as machine learning for UAV design and control applications.



Gim Song Soh received the M.Sc. and Ph.D. degrees in mechanical and aerospace engineering from the University of California (UCI) Irvine, Irvine, CA, USA, in 2006 and 2008, respectively.

He researched and developed innovative computer aided design software tools for the invention of articulated mechanical systems with UCI. He is currently an Associate Professor with the Engineering Product Development (EPD) Pillar, Singapore University of Technology and Design (SUTD), Singapore. His research interests lie on mechanism and robotics with emphasis on its design, kinematics, and biomechanics.



Shaohui Foong received the B.S., M.S., and Ph.D. degrees in mechanical engineering from the George W. Woodruff School of Mechanical Engineering, Georgia Institute of Technology, Atlanta, GA, USA, in 2005, 2008, and 2010, respectively.

In 2011, he was a Visiting Assistant Professor with the Massachusetts Institute of Technology, Cambridge, MA, USA. He is an Associate Professor with the Engineering Product Development (EPD) Pillar, Singapore University of Technology and Design (SUTD), and a Visiting Academician with Changi General Hospital, Singapore. His research interests include system dynamics and control, nature-inspired robotics, magnetic localization, medical devices, and design education and pedagogy.